LAWRENCE
LIVERMORE
NATIONAL
LABORATORY

UCRL-CONF-211403

SPH and Material Failure: Progress Report

J. M. Owen

April 15, 2005

Joint Russian American 5 Laboratory Conference on
Computational Mathematics/Physics
Vienna, Austria
June 19, 2005 through June 24, 2005

Disclaimer

SPH and Material Failure: Progress Report

J. Michael Owen

April 7, 2005

Smoothed Particle Hydrodynamics (SPH) is a meshless Lagrangian technique for modeling hydrodynamics, and as such offers some unique advantages when applied to problems of material failure and breakup. The two most important of these advantages are

- SPH is Lagrangian and robust – i.e., it is never necessary to advect or remap. Damage models typically involve a number of complex history variables (such as the damage associated with the Lagrangian mass, crack orientations, etc.), and advecting these quantities as is required in a mesh based algorithm is a very challenging problem.
- SPH allows the Lagrangian points to move about, reconnect, or separate as dictated by the material flow. This naturally allows for the points to move apart as distinct fragments of material form, resulting in gaps or cracks between the fragments. Typically mesh based algorithms represent the "cracks" between fragments as zones of failed material, which is quite different than allowing voids devoid of material to form.

1 Material modeling

SPH is usually applied to problems of compressible gas dynamics, but equations of state and strength models appropriate for solids can be implemented in the same manner as is done for mesh based algorithms. At this time we have implemented the Gruneisen equation of state and Steinberg-Guinan rate independent strength model in our research SPH code. These have been verified as working correctly via two test problems: a five material flyer plate impact problem with experimental velocity diagnostics (checked against the experiment as well as code to code comparisons; see Figure 1); the Taylor rod impact problem, wherein a metal rod is fired into a solid wall at a few hundred meters per second (these results were verified via code to code comparison, Figure 2). We also have an initial implementation of the Steinberg-Guinan-Lund rate dependent strength model, but this option has not yet been verified.

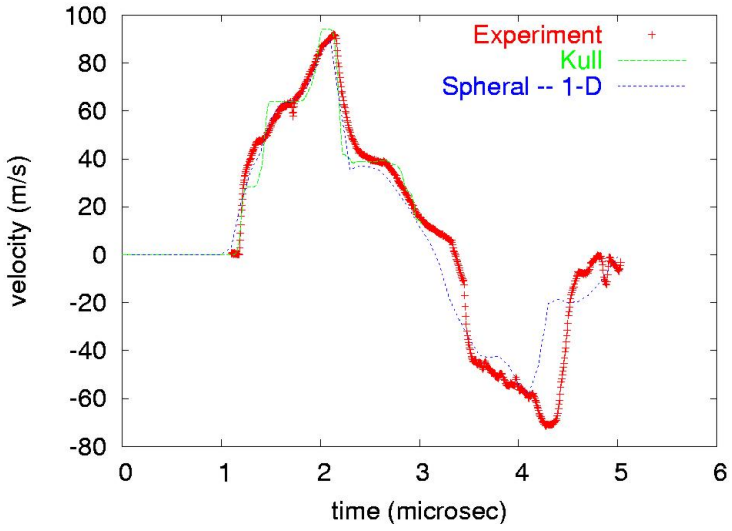

Figure 1: Five material flyer plate impact, velocity diagnostic compared between experiment, SPH (Spheral), and staggered grid Lagrangian (Kull).

2 Fracture modeling

We have implemented a scalar damage model whose application to SPH is described by Benz & Asphaug (1994, 1995, 1999), based on a statistical description of material flaws due to Grady & Kipp (1980). This model assumes that there is a randomly distributed set of flaw activation energies ε_f in a material described by the Weibull distribution

$$n(\epsilon_\Sigma) = k\epsilon_\Sigma^m, \tag{1}$$

where $n(\epsilon_\Sigma)$ is the number density of flaws with activation energies $\varepsilon_f \leq \epsilon_\Sigma$, and k and m are material dependent parameters. In the SPH implementation, a set of flaw activation energies is assigned to each SPH point at problem setup according to this distribution. In an effort to make this flaw assignment as resolution independent as possible we follow the following prescription. For a given strain we expect the weakest flaws to become active and break first – therefore we must ensure the population of weakest flaws is always represented regardless of resolution. For a volume V of material, equation 1 implies there should be a single weakest flaw activation energy: $\min(\varepsilon_f) = 1/(kV)^{1/m}$. We pick an SPH node at random and assign it this flaw activation energy. We then pick another SPH node at random (which could be the same node as previously), and assign it the next weakest activation energy, $2/(kV)^{1/m}$. We proceed in this manner until all nodes have been assigned at least one flaw. Upon completion there will be $N_f \approx N\log(N)$ total flaws assigned, where N is the number of SPH nodes in the material. Figure 3 shows the number of flaws assigned to each node in a volume of steel in this manner, and figure 4 shows how the resulting flaw

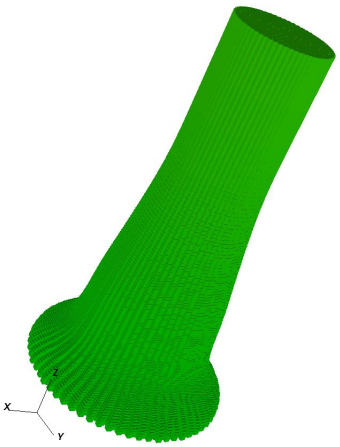

Figure 2: Tantalum "Taylor" rod impact problem @ t = 150 μsec. Initial velocity was 250 m/s, and by 150 μsec the impact has halted.

distribution function $n(\epsilon_\Sigma)$ changes with increasing resolution. The numerically seeded flaws follow the expected Weibull distribution accurately up to a cutoff, beyond which there are no stronger flaws represented. As the resolution is increased we probe the strong flaw distribution further and further, but clearly as intended the weakest population of flaws are always represented.

Once we have initialized the flaw population, how do we evolve the resulting damage to the material? As the simulation is advanced in time the instantaneous strain is measured at each node i

$$\varepsilon_i = \frac{\sigma_{ti}}{E_i}, \tag{2}$$

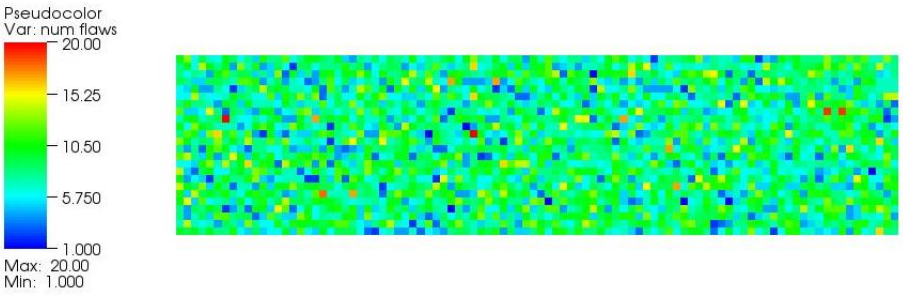

Figure 3: Number of flaws assigned to each node.

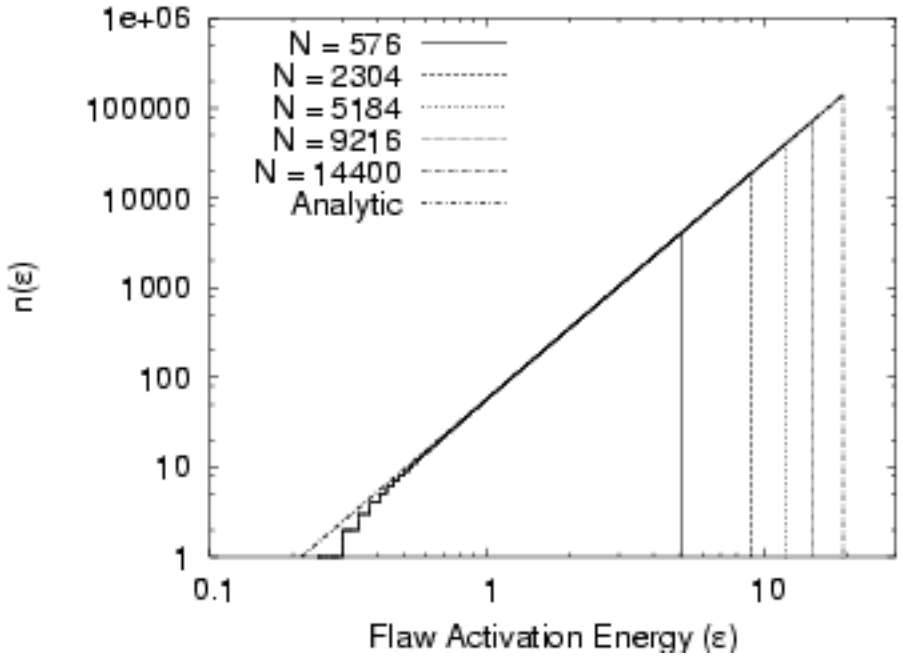

Figure 4: Distribution function of flaw activation energies for a variety of resolutions.

where σ_{ti} is the maximum eigenvalue of the strain tensor $\sigma_i^{\alpha\beta}$ and E_i is Youngs modulus of the SPH node. If ε_i exceeds any of the flaw activation energies associated with the node, it begins to accrue a scalar damage D at the rate

$$\frac{dD_i^{1/3}}{dt} = \frac{c_g}{R_s} = \frac{0.4c_{li}}{\eta_{\max} h_i}, \tag{3}$$

where c_g is the crack growth rate (assumed here to be 0.4 the longitudinal sound speed c_l), and R_s is the radius of the volume in which the strain is relieved by the crack. We equate this volume with the SPH sampling volume, whose radius is determined by the radius of compact support of the interpolation kernel $\eta_{\max} h_i$ (h_i is smoothing scale of the SPH node, and $\eta_{\max}$ is the radius at which the interpolation kernel falls to zero in units of h). The scalar damage is limited to the range $D \in [0, 1]$, where $D = 0$ implies no damage and $D = 1$ implies a fully damaged point.

In the original algorithm Benz & Asphaug apply the damage by scaling properties such as the strength, negative pressure, etc. of a node by factors of $1 - D_i$. In our implementation we choose instead to use D to breed new nodes of a damaged material, which obeys a different equation of state (supporting no negative pressures) and does not possess any strength. The new node masses

are given by

$$m_{Ui} = (1 - D_i)m_{0i}, \quad (4)$$
$$m_{Di} = D_i m_{0i}, \quad (5)$$

where m_{Ui} and m_{Di} are the undamaged and damaged node masses, and m_{0i} is the original mass of node i. The net effect should be the same as the Benz & Asphaug algorithm, but is cleaner in our code. Putting this all together, a typical simulation proceeds something like the following.

1. At startup a population of flaw activation energies ε_f is assigned to each node. This set of flaw activation energies remains fixed for the duration of the problem.

2. As the strain at any given node exceeds these flaw activation energies damage begins to accrue, breeding a new population of damaged nodes which gradually begin to replace the failing nodes of the original material.

3. As nodes entirely fail and are converted to the damaged species, fragments of the undamaged material begin to form and move independently of one and other. These fragments are typically surrounded by the damaged nodes, which freely disperse if sufficient space opens up between the fragments, creating cracks between the dissociated fragments.

2.1 Fragment identification

The SPH algorithm lends itself readily to the identification of individual fragments of material because, rather than assuming a static connectivity, it builds the connectivity between nodes on the fly as required. We can therefore identify fragments as any set of the original undamaged nodes that are still continuously connected – i.e., the connected neighbors of nodes to which I am connected are part of my fragment. We have implemented such an algorithm, the results of which can be seen in Figures 6, 9, & 15 below.

3 Fracture tests

We have tested the fracture model in some idealized test cases: tensile rods undergoing initially uniaxial strain along their length (as though they are being pulled apart by their ends, §3.1), and tensile disks undergoing radial strain such as would occur if the disks were undergoing initially uniform expansion (§3.2). For efficiency these tests are carried out in two dimensional geometry, and therefore don't quantitatively reflect real experiments. However, the Grady-Kipp formalism makes some analytic predictions about the distributions of fragments that should result. Additionally, we have performed one realistic test of a gas gun experiment following the fracture and break up of steel cylinders, described in §3.3.

3.1 Tensile rods

This is a two dimensional test case wherein we take a 20x5 cm steel rod and impose an initially linear velocity field

$$\mathbf{v} = \begin{pmatrix} v_0 x \\ 0 \end{pmatrix}, \tag{6}$$

which creates a constant strain rate $\dot{\varepsilon}$ in the rod. The velocity of the nodes on the extreme ends of the rod is forced to remain constant throughout the simulation, ensuring that however slowly the rod is pulled apart it will ultimately break.

For the case of constant strain rate, the Grady-Kipp formalism predicts an expected most probable fragment size as

$$L(\dot{\varepsilon}) = \frac{6c_g}{m+2}\alpha^{1/(m+3)}\dot{\varepsilon}^{-m/(m+3)}. \tag{7}$$

In the two strain cases we consider below ($v_0 = 10$ m/s and $v_0 = 100$ m/s), this predicts typical fragment sizes of 8.6 cm and 2.9 cm, respectively.

3.1.1 $v_0 = 10$ m/s

(a) 100x25

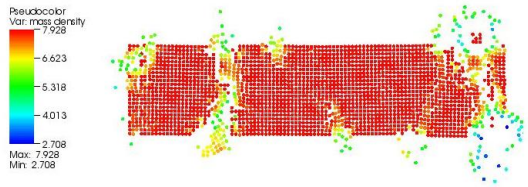

(b) 200x50

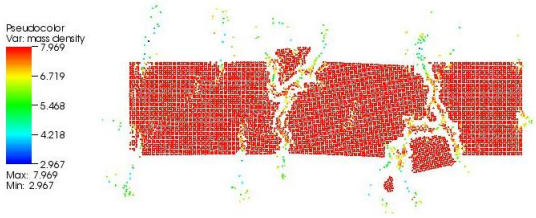

(c) 400x100

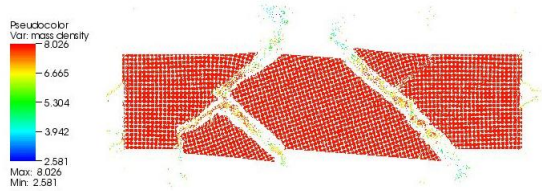

Figure 5: Mass density for the $v_0 = 10$ m/s tensile steel rods at $t = 500\mu$sec. Shown are the (a) 100x25, (b) 200x50, and (c) 400x100 node resolution cases.

We consider three different resolutions of this problem (100x25, 200x50, and 400x100 nodes), in an effort to examine the resolution dependence of the resulting fragment distribution. Figure 5 plots the nodes colored by mass density at $t = 500\mu$sec; each of the simulations shows the rod breaking into roughly

2-3 major pieces as equation 7 predicts (recall the most probably fragment size predicted is ~ 8.9 cm.) The lower density nodes between the fragments are the failed nodes which no longer can go into tension in response to the density falling below the reference density of steel, so these regions take up the expansion and relieve the strain on the surviving steel fragments. This can be seen even more clearly in Figure 6, which plots the surviving steel nodes colored by fragment index as identified by the algorithm described in §2.1. It is interesting to note that as we increase the resolution in the simulations, the breaks in the rod straighten up into roughly 45° breaks. This appears to be due to the strain or extension in the rod being concentrated into a few diagonal bands near the ends of the rod as the extension continues. Outside of these bands the material nearly stops stretching as the material strength overcomes the extensional force, concentrating all the distortion and shear into these few well defined bands. It is along these bands that the strain rises and the breaks occur when the fragmentation model is applied.

(a) 100x25

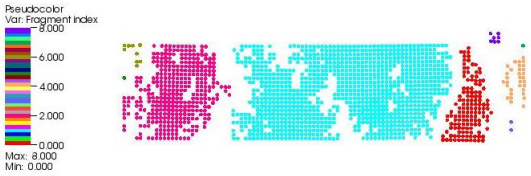

(b) 200x50

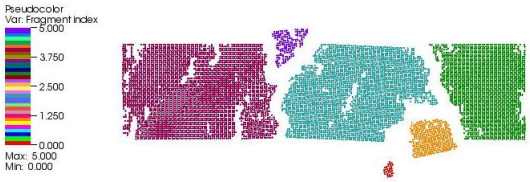

(c) 400x100

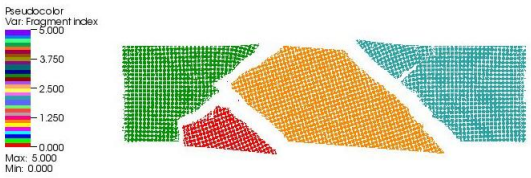

Figure 6: Identified fragments in the $v_0 = 10$ m/s tensile steel rods at $t = 500\mu$sec. Shown are the (a) 100x25, (b) 200x50, and (c) 400x100 node resolution cases.

Figure 7 plots the cumulative mass distribution function of the fragments, i.e., the total mass contained in fragments of a given mass or less. The masses in this figure are normalized to the total mass in the initial rod, and failed nodes are counted as individual fragments in order to ensure the total mass sum is the same for all three simulations. It appears that the mass distribution function of the fragments converges (at least in the intermediate and high resolution simulations), which is consistent with the qualitative observation that the bar breaks into roughly the same number of major fragments in each case. This

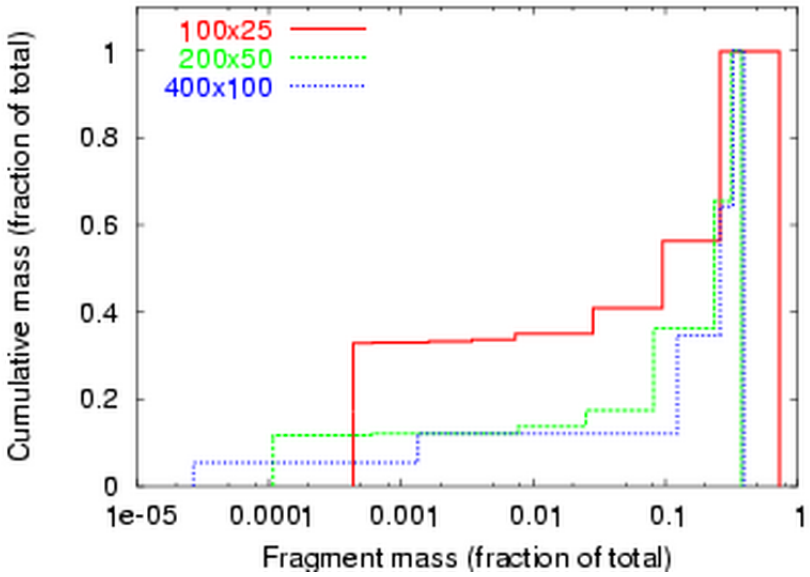

Figure 7: Cumulative mass distribution of fragments in the $v_0 = 10$ m/s tensile steel rods at $t = 500\mu$sec. Failed nodes are counted as individual fragments for mass conservation.

convergence in the mass properties seems to be fairly independent of how well the occurrence of shear bands is resolved.

3.1.2 $v_0 = 100$ m/s

In this version of the tensile rod test case we increase v_0 from 10 to 100 m/s, effectively increasing the strain rate by a factor of 10. The Grady-Kipp formalism now predicts a much smaller typical fragment size (~ 2.9 cm), and this qualitatively concurs with what we see in the plots of the nodes colored by mass density in Figure 8. Looking at the remaining steel nodes in identified fragments (Figure 9), we can see the majority of the nodes in the lowest resolution case have simply turned into unresolved fully damaged "dust", while the intermediate and high-resolution cases have at least maintained some recognizable fragments. Qualitatively we again see that as we increase resolution the cracks become straighter and more diagonal, though there are now many more of them. Considering the cumulative fragment mass distribution function in Figure 10, it does not appear the fragment distribution has converged even in this simple gross measure in any of our runs, suggesting that for this higher strain rate case we need to go to even higher resolution before we can expect to see convergence in these fragment properties.

(a) 100x25

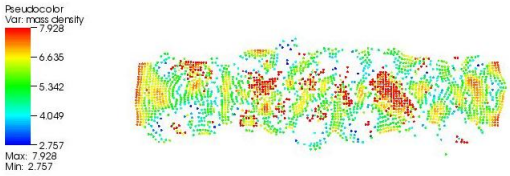

(b) 200x50

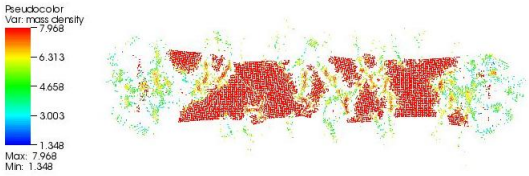

(c) 400x100

Figure 8: Mass density for the $v_0 = 100$ m/s tensile steel rods at $t = 500\mu$sec. Shown are the (a) 100x25, (b) 200x50, and (c) 400x100 node resolution cases.

3.1.3 Strain – why do the rods break where they do?

It is interesting to examine the history of the strain in these simple tensile rod test cases to see how the material winds up breaking where it does, and why. Figure 11 plots the nodes in the intermediate resolution $v_0 = 10$ m/s test case colored by the strain (Eq. 2) at three time slices: 37.5, 62.5, and 100 μsec. At the early time we can see that the strain is rising fairly uniformly throughout the rod, with some variation due to the differing damage that is being done to the nodes in accordance with variation in the flaw activation energies. By 62.5 μsec, the strain has risen to the point that the first fully failed nodes have formed in the upper left quadrant. You can see around these failed nodes that the strain is increased at the tips of the "crack", and decreased along the edges of the crack. This is due to the nodes at the ends of the crack taking up the extensional strain holding the bar together, and the nodes on either side of the crack having their strain relieved because they no longer communicate with unfailed nodes across the far side of the crack and therefore do not see the velocity differential. This pattern will naturally cause the crack to propagate at the tips and relieve failure on either side of the crack, as we would physically expect. At 100 μsec the cracking process has progressed much further – the blue relieved areas where the strain has been largely alleviated have swept out away from the forming cracks, which have nearly extended across the width of the bar.

(a) 100x25

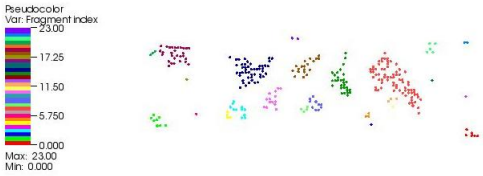

(b) 200x50

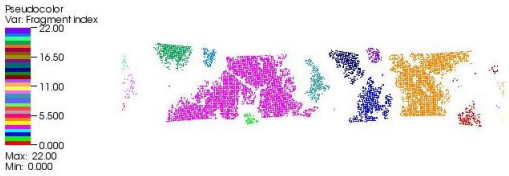

(c) 400x100

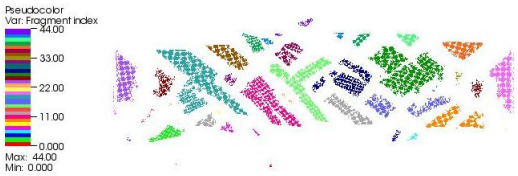

Figure 9: Identified fragments in the $v_0 = 100$ m/s tensile steel rods at $t = 500\mu$sec. Shown are the (a) 100x25, (b) 200x50, and (c) 400x100 node resolution cases.

3.2 Tensile disks

We now consider a test case with biaxial strain. We take a steel disk (again in two dimensions) and impose an initial radial velocity field according to $v_r = v_0 r$. The steel disk is 10 cm in radius, and we choose $v_0 = 100$ m/s – this is a higher strain rate case than the tensile rods we considered in the previous section. We also do not impose a forced boundary condition on the outer regions of the disk, so the strength of the steel is allowed to slow the expansion.

Figure 12 shows the nodes colored by mass density at $t = 25\mu$sec for two different resolutions: n_r (number of radial nodes) = 100 and 200. In each radial ring the nodes are spaced azimuthally with the same spacing as in radius, so that there are approximately four times as many nodes in the high resolution simulation as there are in the low resolution case. As in the tensile rod case, the low resolution nodes are the failed material which is now taking up the expansion of the disk. Despite the resolution difference qualitatively the pattern of failure in both simulations is quite similar: the failed regions appear wider in the low resolution case because the cracks must fail approximately four nodes across to break communication in the unfailed material across the crack and relieve strain. The higher resolution simulation simply resolves this four node spacing on smaller scales. Unlike the tensile rod tests, in this case the failed material has no way to escape the system because the outer portion of the disk has not failed yet – there is no way for the fragments to separate and release the failed nodes.

Figure 13 plot the nodes at the same time colored by radial velocity. We

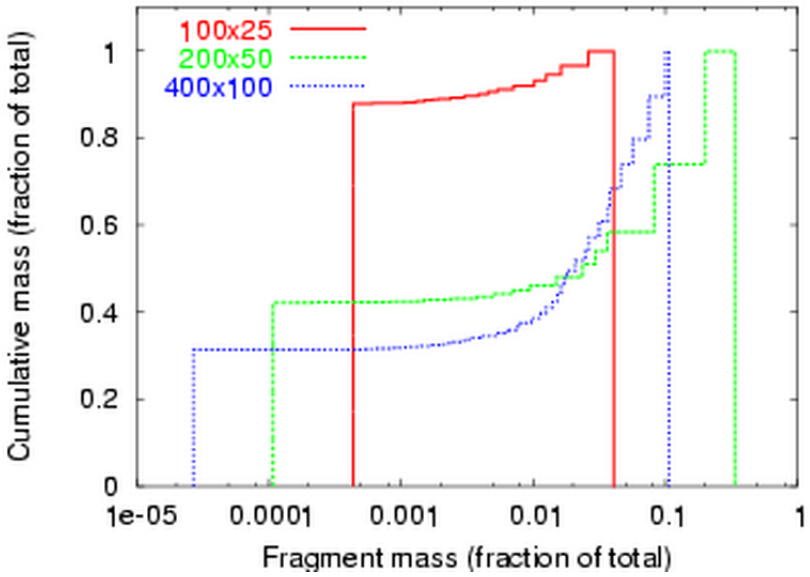

Figure 10: Cumulative mass distribution of fragments in the $v_0 = 100$ m/s tensile steel rods at $t = 500\mu$sec. Failed nodes are counted as individual fragments for mass conservation.

can see in this figure that the outer portions of the disk have ceased expansion and are in fact recompressing. Therefore the failure in the disk has by this time essentially halted and the crack pattern is frozen in. Figure 14 shows the nodes colored by damage D. It is clear that there is extensive damage throughout the disk by this time. We know from other simulations if we push the initial expansion velocity much higher (say $v_0 = 150$ m/s, then the disk essentially vaporizes into failed nodes.

Figure 15 plots the fragments that are identified in the two simulations. We can see that although the failure pattern in the two is quite similar, the lower resolution run was able to form more distinct fragments. The cracks in the intermediate radii in the high resolution run did not connect and build distinct fragments, resulting in a different fragment distribution. We can see a minor effect due to this on the cumulative fragment mass distribution function in Figure 16, though both are dominated by the single large "fragment" consisting of the outer regions of the disk. The fragment distribution function is quite similar between the two cases, if we factor out the difference in the first step of the function due to the differing node masses in the failed material which makes up the lowest mass "fragments."

(a) 37.5 μsec

(b) 62.5 μsec

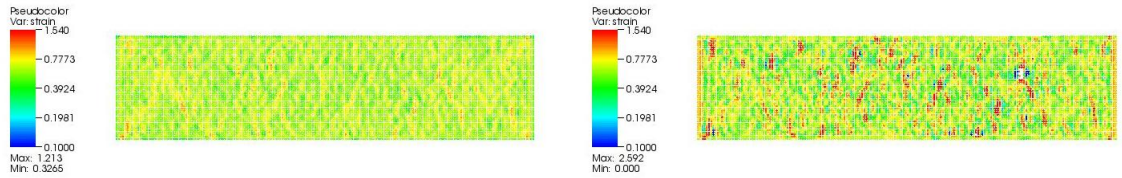

(c) 100 μsec

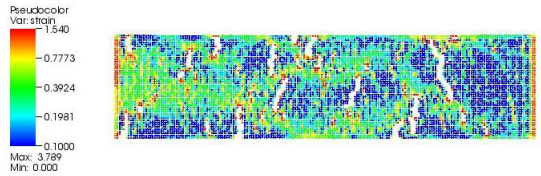

Figure 11: Strain at three different times for 200x50 $v_0 = 10$ m/s tensile steel rod.

3.3 Expanding tube

Our final test case is a three-dimensional model of a published gas gun experiment (Vogler et al. 2003). In this problem a cylindrical steel tube (5 cm long, 12.7 mm in diameter, with a 3 mm wall thickness) is placed against the anvil at the barrel of a gas gun. A lexan plug half the length of the tube is inserted in the tube on the anvil end, while a another equal length lexan projectile is fired into the tube at 1.92 km/s (see Figure 17 for a picture of the initial material setup in this problem). When the projectile impacts on the lexan plug within the tube, the two compress in length and expand in circumference against the inside of the tube, causing it to expand in radius. The steel tube is stretched and ultimately fails, breaking into fragments. There are a number of diagnostics available for this experiment (high speed photography of the breakup, VISAR velocity data on the expansion of the tube at several points, soft-capture of the fragments for experimental determination of the fragment properties, etc.), which makes this problem an appealing test case for models of fragmentation.

Figure 18 shows the velocities of the various materials during the initial entry of the projectile into the steel tube and impact of the projectile on the lexan plug. These velocities are colored logarithmically to enhance the visualization of the disturbance propagating through the system during this early evolution. As the projectile transits down the tube it scrapes the inner surface, causing some damage on this surface before the impact on the plug occurs.

Figure 19 shows the state of the system at $t = 26.75\mu$sec, which is as far as the simulation had advanced at this writing. In panel (a) you can clearly see the lexan plug and projectile have expanded against the surrounding steel tube,

(a) $n_r = 100$ (b) $n_r = 200$

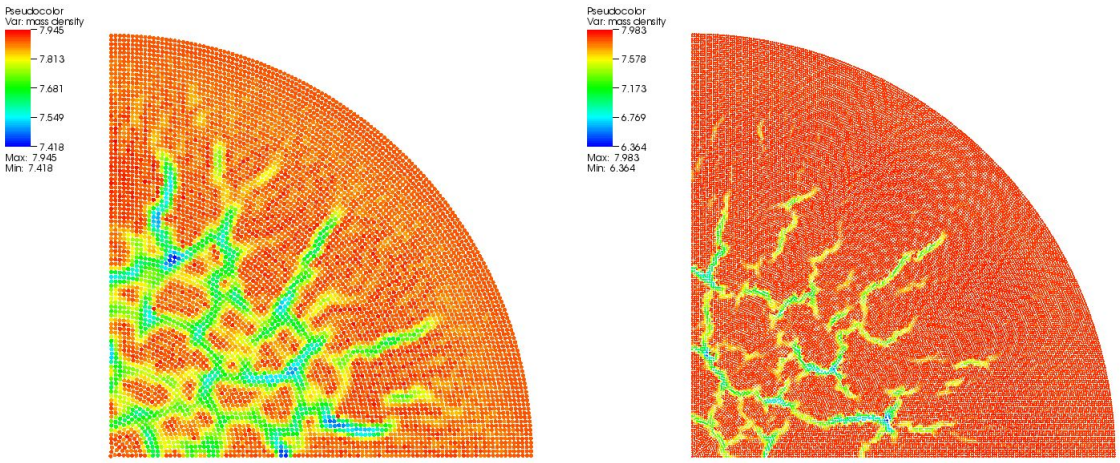

Figure 12: Mass density at $t = 25\mu$sec in one quadrant of the tensile disk. Two simulations are shown: (a) uses 100 nodes in radius, while (b) uses 200.

distending it significantly. Panel (b) shows the mass density of the damaged steel (which at this point is still entirely coexistent with the undamaged steel). In this panel we can clearly see the thin shell of damaged material (on the right side) caused by the entry of the projectile into the tube, while the majority of the damage is in the expanding central portion of the tube. Panels (c) & (d) show the velocity of the undamaged material, in which we can just see the beginning of a fully failed rupture through the tube near the center of the expansion. Note also the trough in the velocity on the left-hand (anvil) side of the tube. This is part of a wave or ripple that is propagating down the tube from the central expansion point, which will be significant in the interpretation of the VISAR data below.

Figure 20a depicts the positions the three VISAR velocity measurements were made at in the experiment. In order to compare the SPH simulation to these measurements, we averaged the radial motion of all the nodes on the surface of the tube at these positions, resulting in the time history comparison in Figure 20b. The simulations follow the bulk properties of these velocity curves, but show a significant ringing or oscillation around the experimental values. Recall in Figure 19 we noted the presence of a wave propagating down the length of the tube from the expansion point – this wave seems to be responsible for the variation we're seeing in the simulated VISAR data, and it is not present in the

(a) $n_r = 100$ (b) $n_r = 200$

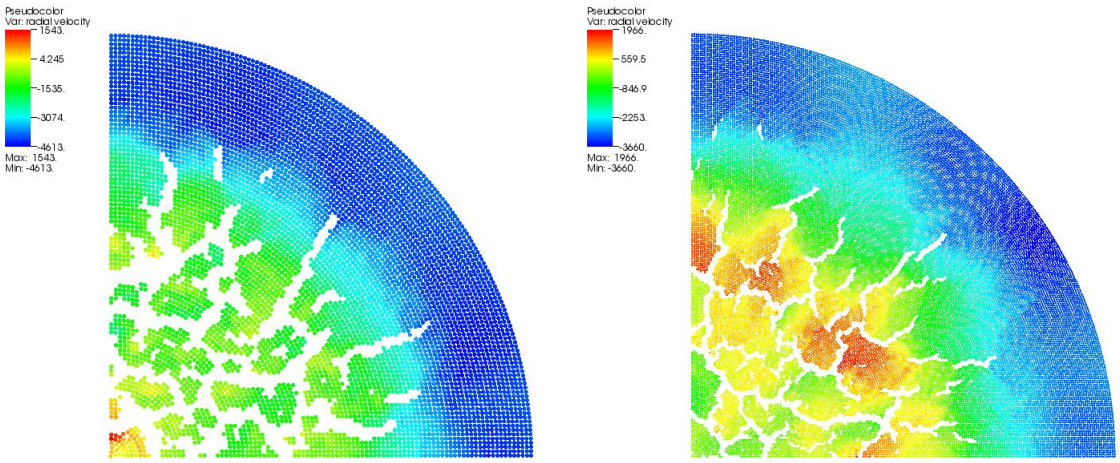

Figure 13: Radial velocity at $t = 25\mu$sec in one quadrant of the tensile disk simulations. Note that the outermost radii have turned around.

experiment. Our current interpretation is that this error in the simulation is likely due to problems in our material modeling. Possibly the rate-independent Steinberg-Guinan strength model is not appropriate at these strain rates – the cause of this discrepancy remains under investigation.

4 Summary and future work

We have reported on the current status of an ongoing investigation into the utility of SPH in modeling problems of material failure and fracture. We have implemented standard analytic equations of state and strength models to model the hydrodynamic response of solids, and a simple published failure model due to Benz & Asphaug (1994, 1995, 1999) to model fracture and breakup of those materials. We have tested this fracture model with idealized test problems (tensile rods and disks), and one realistic model of a gas gun experiment. These tests so far indicate that our results are qualitatively reasonable, though the VISAR velocity comparison for the gas gun experiment shows that our material modeling needs some improvement. Future work we intend to pursue includes

- Apply these techniques to a wider variety of test problems.
- Implement improved strength modeling and test whether this improves

(a) $n_r = 100$ (b) $n_r = 200$

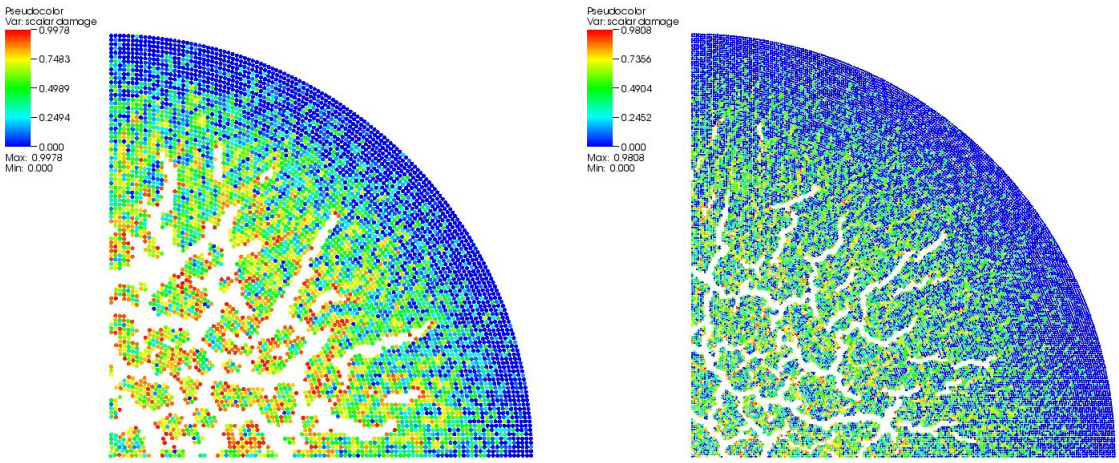

Figure 14: Scalar damage D at $t = 25\mu$sec in one quadrant of the tensile disk simulations. Recall $D \in [0, 1]$, with $D = 0$ an entirely undamaged node and $D = 1$ a fully damaged node.

the match with the experimental data in the gas gun experiment.

- Implement a wider variety of material failure models.
- Incorporate the fragment identification algorithm into the run time scheme, so that fragments can be identified and spun off as new materials during the coarse of a run. This is necessary due to the fact that, because SPH is a continuously reconnecting algorithm, in the current implementation if two distinct fragments of the same material collide they will reconnect, and strength will take effect nonphysically between the fragments again.
- Assorted numerical improvements: improved treatment of of surfaces; use of the summed mass density definition rather time integrated; application of ASPH (Adaptive Smoothed Particle Hydrodynamics); etc.

This work was performed under the auspices of the U.S. Department of Energy by the University of California Lawrence Livermore National Laboratory under contract No. W-7405-Eng-48.

(a) $n_r = 100$ (b) $n_r = 200$

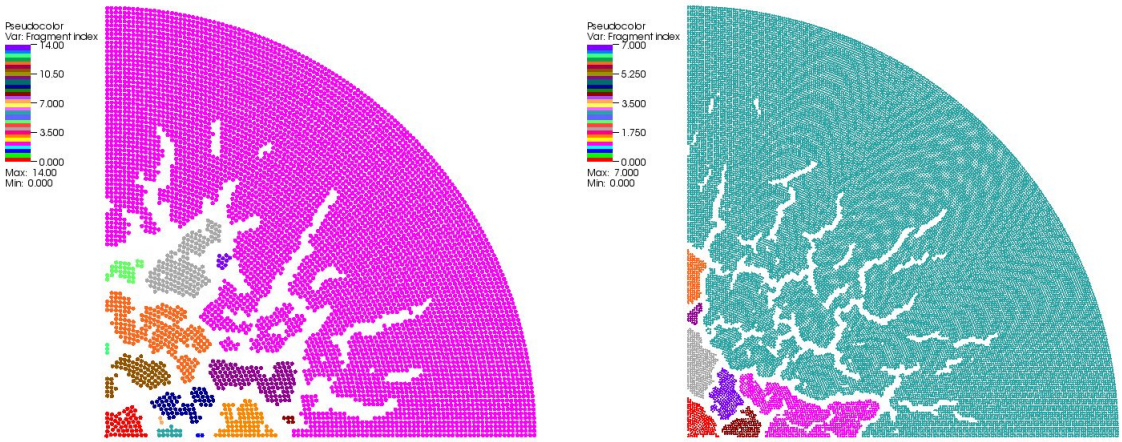

Figure 15: Fragments identified in the tensile disk simulations.

References

[1] Benz, W., & Asphaug, E., *Icarus*, **107**, 98-116 (1994).

[2] Benz, W., & Asphaug, E., *Comp. Phys. Comm.*, **87**, 253-265 (1995).

[3] Benz, W., & Asphaug, E., *Icarus*, **142**, 5-20 (1999).

[4] Grady, D.E., & Kipp, M.E., *Int. J. Rock Mech. Min. Sci. Geomech. Abstr.*, **17**, 147-157 (1980).

[5] Vogler, T.J., Thornhill, T.F., Reinhart, W.D., Chhabildas, L.C., Grady, D.E., Wilson, L.T., Hurricane, O.A., & Sunwoo, A., *Int. J. of Impact. Eng.*, **29**, 735-746 (2003).

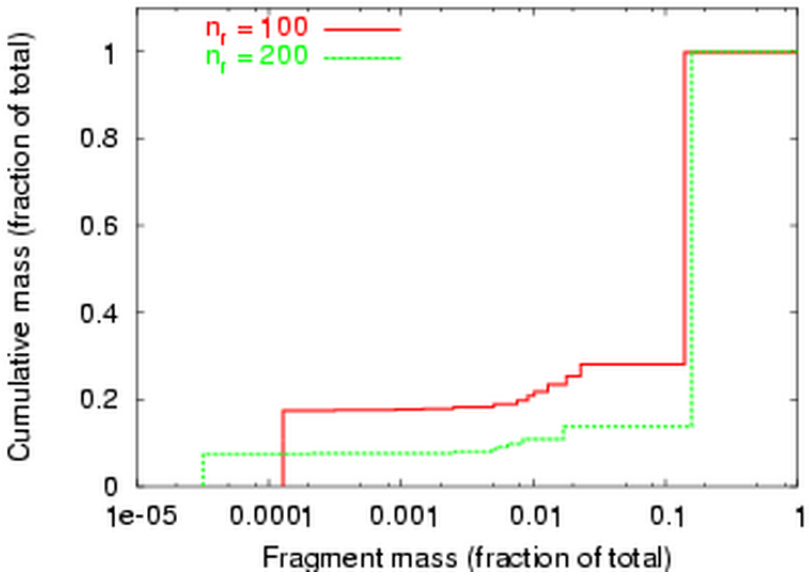

Figure 16: Cumulative mass distribution of fragments in the tensile disk simulations at $t = 25\mu$sec.

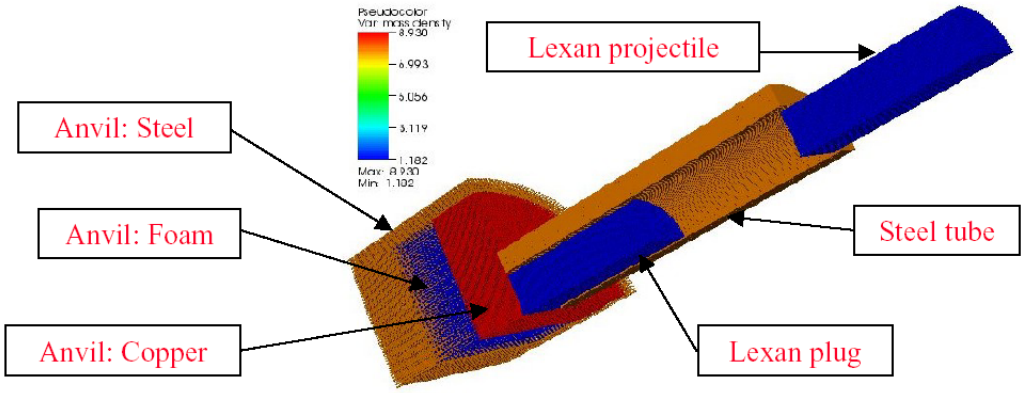

Figure 17: Initial material distribution in gas gun expanding tube experiment.

(a) $t = 8\mu$sec

(b) $t = 13.75\mu$sec

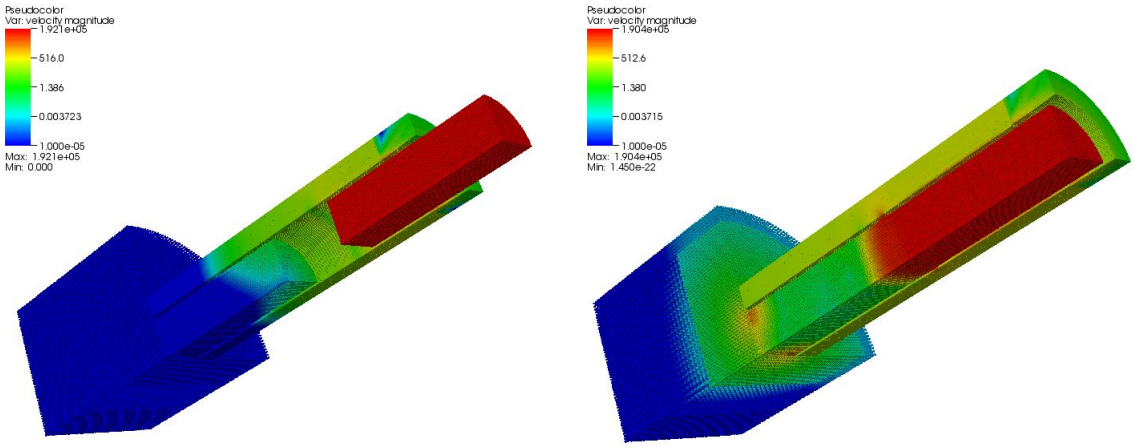

Figure 18: Velocities in the gas gun simulation during projectile entry into the steel tube.

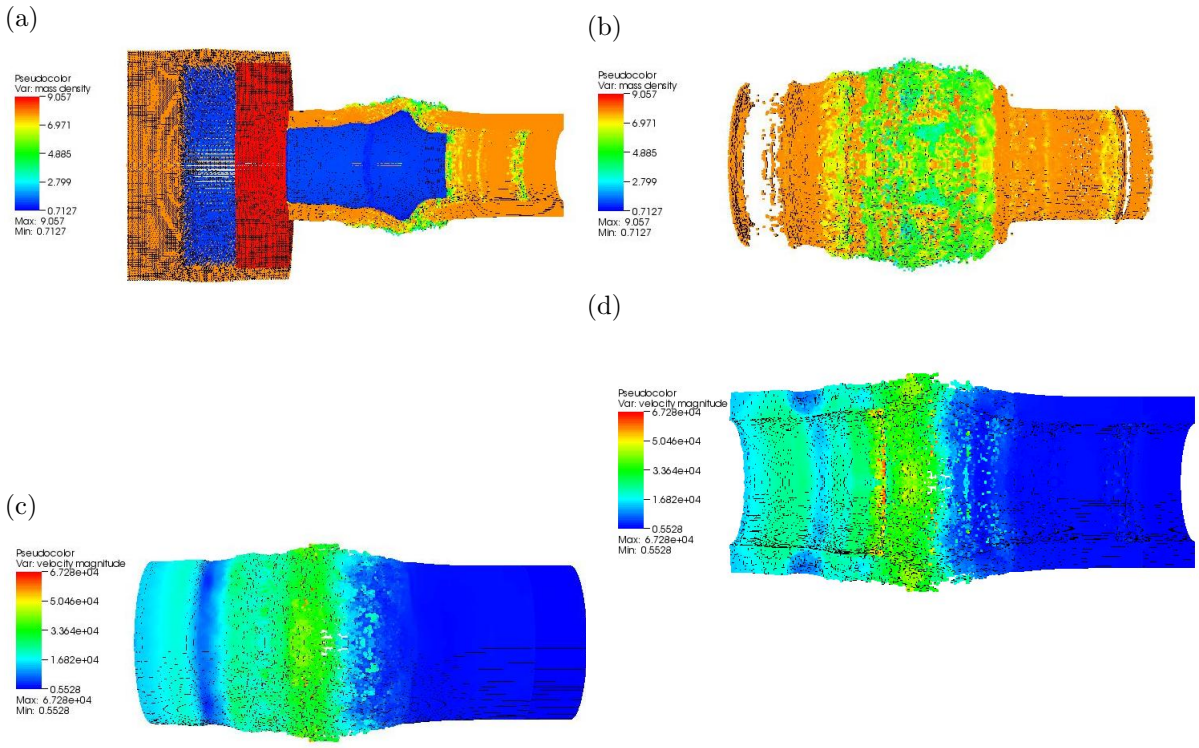

Figure 19: State of the expanding tube simulation @ $t = 26.75\mu$sec. Shown are (a) mass density of all materials from the interior; (b) mass density of the damaged steel from the exterior; (c) velocity of the undamaged steel (exterior view); (d) velocity of the undamaged steel (interior view).

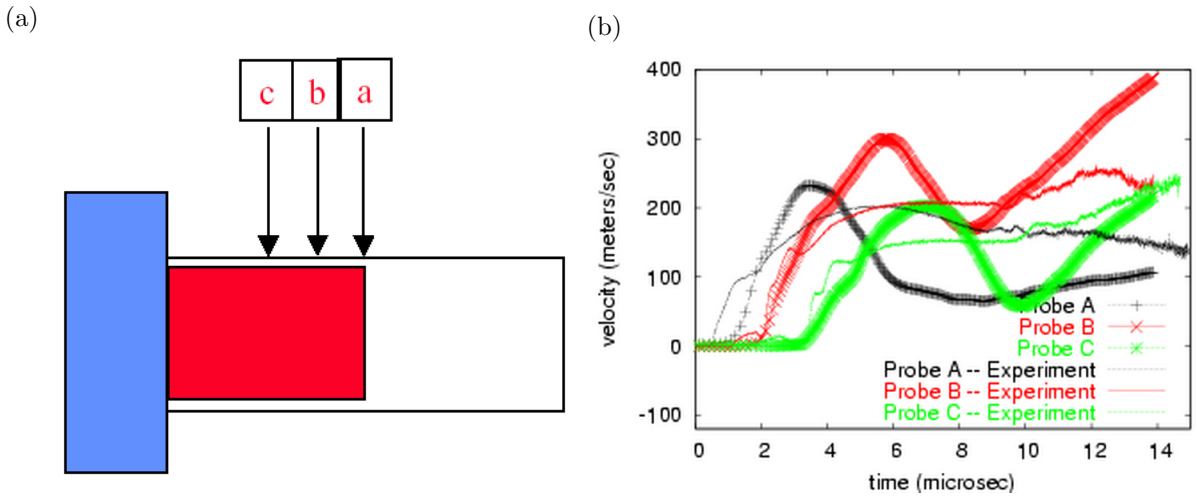

Figure 20: VISAR velocity data for the expanding tube gas gun experiment. Panel (a) depicts the positions of the three VISAR probes along the tube: probes A, B, & C at 25, 20, & 15 mm from the anvil, respectively. Panel (b) shows the time history of the VISAR measurements, comparing experiment to the SPH simulation.